

CoTe₂: A Quantum Critical Dirac Metal with Strong Spin Fluctuations

Peter E. Siegfried, Hari Bhandari, Jeanie Qi, Rojila Ghimire, Jayadeep Joshi, Zachary T. Messegee, Willie B. Beeson, Kai Liu, Madhav Prasad Ghimire, Yanliu Dang, Huairuo Zhang, Albert V. Davydov, Xiaoyan Tan, Patrick M. Vora, Igor I. Mazin, and Nirmal J. Ghimire*

Quantum critical points separating weak ferromagnetic and paramagnetic phases trigger many novel phenomena. Dynamical spin fluctuations not only suppress the long-range order, but can also lead to unusual transport and even superconductivity. Combining quantum criticality with topological electronic properties presents a rare and unique opportunity. Here, by means of *ab initio* calculations and magnetic, thermal, and transport measurements, it is shown that the orthorhombic CoTe₂ is close to ferromagnetism, which appears suppressed by spin fluctuations. Calculations and transport measurements reveal nodal Dirac lines, making it a rare combination of proximity to quantum criticality and Dirac topology.

of topological insulators, then expanded to semimetals, first to 3D Dirac and Weyl points^[1] and even to metals,^[2–9] leading to unusual magnetotransport properties. The novel physics and rarity of these states, as well as their potential applications^[10–12] have been at the forefront of recent research. This said, more often than not it is difficult to see the effect of topologically non-trivial points in metals because they tend to be shadowed by other, trivial parts of the Fermi surface. In this connection, a search has been underway for metals that possess symmetry-driven planes of degeneracy in the momentum space, which can cross

the Fermi level and generate continuous nodal lines of Dirac points directly at the Fermi level.^[13] Such metals would have a dramatically larger part of the Fermi surface bearing topological phenomena, and thus have potential for more unusual properties such as 3D quantum anomalous Hall effect,^[5,14] tunable Weyl points^[15], and “drumhead” surface states^[16] that are argued to provide a route to higher temperature superconductivity.^[17]


1. Introduction

In condensed matter physics, interplay between ionic, electronic, and magnetic degrees of freedom can generate many novel phenomena and quasiparticle excitations. Of particular interest have been topologically protected (i.e., by symmetry) band crossings and other electronic features. The field started with the study

P. E. Siegfried, H. Bhandari, J. Joshi, P. M. Vora, I. I. Mazin, N. J. Ghimire
Department of Physics and Astronomy
George Mason University
Fairfax, VA 22030, USA
E-mail: nghimire@gmu.edu

P. E. Siegfried, H. Bhandari, J. Joshi, P. M. Vora, I. I. Mazin, N. J. Ghimire
Quantum Science and Engineering Center
George Mason University
Fairfax, VA 22030, USA

J. Qi
Thomas Jefferson High School
Alexandria, VA 22312, USA

 The ORCID identification number(s) for the author(s) of this article can be found under <https://doi.org/10.1002/adma.202300640>.

© 2023 The Authors. Advanced Materials published by Wiley-VCH GmbH. This is an open access article under the terms of the Creative Commons Attribution-NonCommercial-NoDerivs License, which permits use and distribution in any medium, provided the original work is properly cited, the use is non-commercial and no modifications or adaptations are made.

R. Ghimire, M. P. Ghimire
Central Department of Physics
Tribhuvan University
Kirtipur, Kathmandu 44613, Nepal

Z. T. Messegee, X. Tan
Department of Chemistry and Biochemistry
George Mason University
Fairfax, VA 22030, USA

W. B. Beeson, K. Liu
Physics Department
Georgetown University
Washington, DC 20057, USA

Y. Dang, H. Zhang, A. V. Davydov
Materials Science and Engineering Division
National Institute of Standards and Technology (NIST)
Gaithersburg, Maryland 20899, USA

H. Zhang
Theiss Research, Inc.
La Jolla, CA 92037, USA

DOI: 10.1002/adma.202300640

Coexistence or proximity of such topological states with other exotic phenomena such as non-trivial spin textures, superconductivity, or quantum criticality can further provide a new route to the properties expected from the interplay of real and momentum space topology, originally discussed in the A-phase of ^3He .^[18,19] These promising theoretical proposals have driven and guided recent experimental efforts toward the realization and study of such materials.

Quantum criticality, in particular, zero-temperature magnetic phase transitions, is believed to have connections to several emergent phenomena such as triplet superconductivity,^[20] non-Fermi liquid scalings^[21] and unusual magnetotransport behavior.^[22] Some famous examples of such materials are unconventional superconductors (Sr_2RuO_4 and Fe-based superconductors), skyrmionic materials (MnSi and FeSi) and weak itinerant ferromagnet, and superparamagnets (ZrZn_2 , Ni_3Al , Ni_3Ga , Pd). As such, a quantum critical system with a substantial presence of topologically nontrivial states at the Fermi level would provide a novel materials platform for the study of the effect of quantum criticality on the topologically protected bands, but such materials are quite rare.

In this work, we report the synthesis, and transport properties of single-crystal CoTe_2 together with the first principle calculations, and argue that it is a quantum critical Dirac metal with Dirac points and multiple nodal lines at the Fermi surface. The material does not show magnetic ordering down to 1.8 K despite the DFT ground state being distinctly ferromagnetic, a hallmark of a magnetic order suppressed by quantum-critical spin fluctuation. We find that CoTe_2 is well described by Moriya's self-consistent renormalization theory (SCRT),^[23] further supporting the conclusion that CoTe_2 is close to a ferromagnetic quantum critical point. This is highly interesting for its potential for tuning magnetic correlations in the presence of a unique topological electronic behavior.

2. Results and Discussion

Single crystals of CoTe_2 were grown using the Te self flux method as described in the Experimental Section. CoTe_2 has previously been reported in three different space groups^[24–27] so the structure of our bulk crystals was verified using multiple complementary methods: powder and single-crystal X-ray diffraction, atomic resolution scanning transmission electron microscopy (STEM), and Raman spectroscopy, all confirming the orthorhombic marcasite structure in space group $Pn\bar{m}$ (#58) consistent with the results in ref. [27] (see Sections S1–S3, Supporting Information, for a full structural description).^[28]

We first start by summarizing the electronic band structure of CoTe_2 . **Figure 1** shows the scalar-relativistic (no spin-orbit coupling) band structure along high-symmetry directions and the Fermi surface. The former, depicted in Figure 1a, shows a surprisingly large number of degenerate bands, namely along the X–S–Y, Z–U–R–T–Z, X–U, S–R, and Y–T lines. To understand this, we recall that CoTe_2 crystallizes in an interesting orthorhombic symmetry, $Pn\bar{m}$ (#58). This symmetry group is highly asymmetric: of its 8 symmetry operations half are glide planes. As a result, it has a large number of nodal lines and planes, where all electronic states are doubly degenerate by

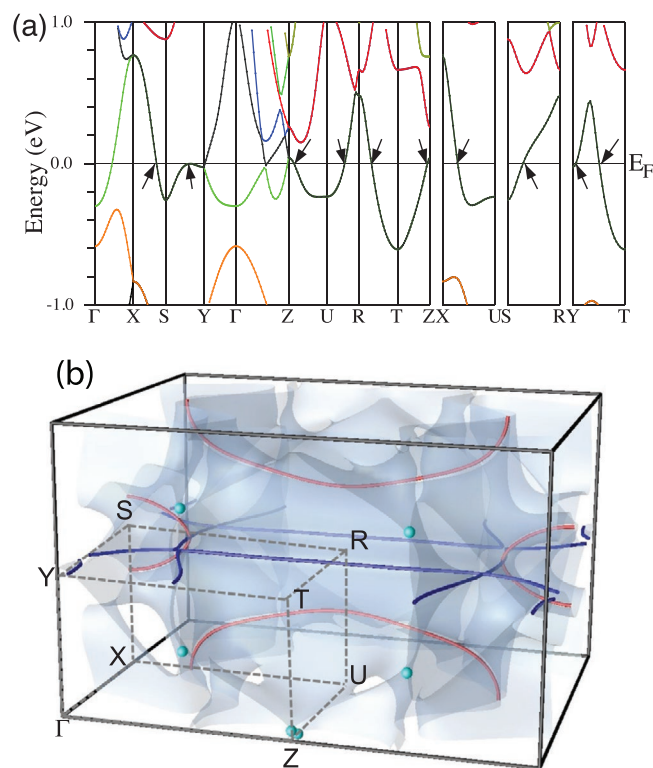


Figure 1. a) Calculated band structure for CoTe_2 . The arrows indicate locations of the Fermi-level Dirac points on these lines, and directions of linear dispersion (see more in Section S4, Supporting Information). b) The Fermi surface in the first reciprocal lattice cell (from Γ to Γ in all directions) with red and blue tubes showing two types of the Dirac nodal lines and cyan balls indicating Dirac points (except near the top Z point).

symmetry. Leonhard et al. analyzed all orthorhombic groups^[13] and concluded that for this group there are two such planes, defined by the conditions $k_x = \pi/a$ and $k_y = \pi/b$, respectively, and two lines, Z–T and Z–U. Degenerate planes generate nodal lines on the Fermi surface, which in CoTe_2 form two closed loops (shown in Figure 1b as red loops) in the $k_x = \pi/a$ plane and two sets of intersecting infinite lines, plus a small loop around Y (blue) in the $k_y = \pi/b$ one. The two lines identified in ref. [13] generate two nodal points, shown as two cyan balls near Z in the same figure (note that while these form a quartet of four degenerate points near Z, they do not form, in agreement to the theoretical predictions,^[13] a closed loop). To the best of our knowledge this is the first direct verification of the ref. [13]'s predictions for the $Pn\bar{m}$ space group. Note that in agreement with ref. [13], the degeneracy is lifted linearly in all directions, providing a large phase space for the Dirac electrons.

In addition, there is a line of accidental degeneracy, where two particular bands of Co origin are allowed to cross (without hybridization) in the $k_x = 0$ plane. This line intersects with the Fermi surface at a Dirac point (DP) that sits close (but not exactly at) the center of the Γ –Y–T–Z rectangle, and is also shown in Figure 1b by a cyan ball. This Dirac point is 3D (the degeneracy is lifted linearly in all directions) and strongly tilted.

Last but not least, there is one other special Dirac point in the system. From the topological (in classical sense) point of view an isolated Dirac crossing, by definition, only shows

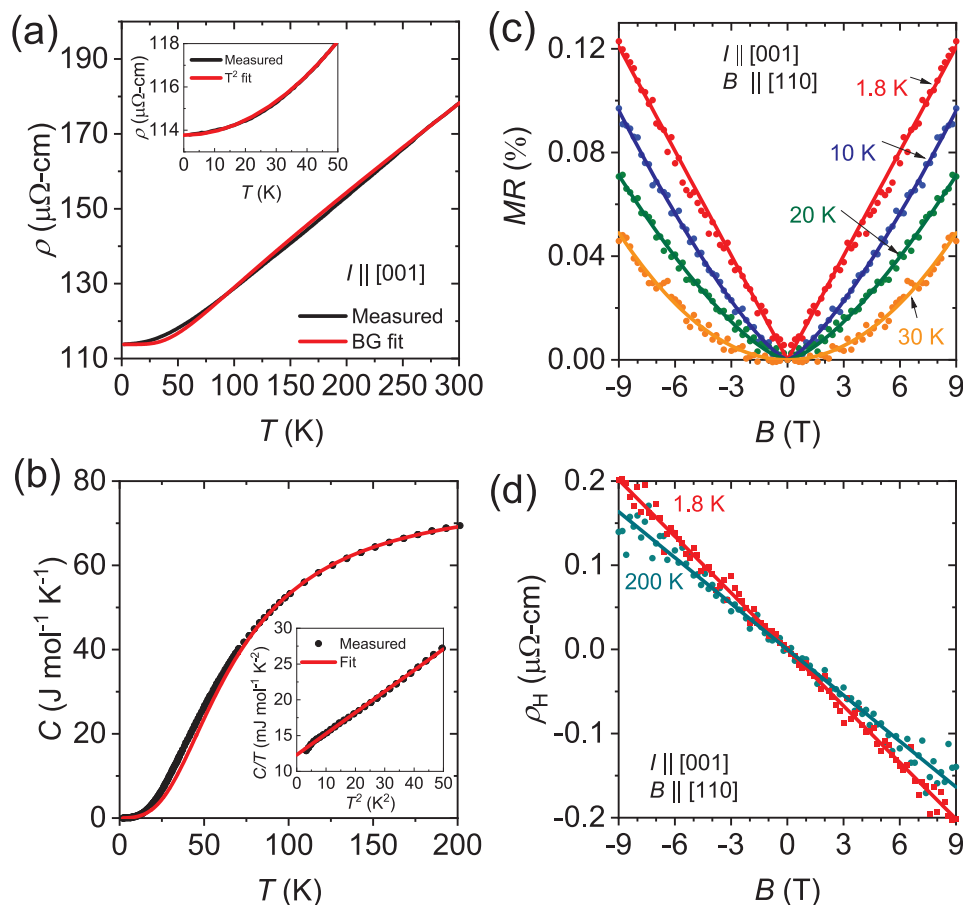


Figure 2. a) Temperature dependence of electrical resistivity (black) and Bloch–Grüneisen fit (red) of CoTe₂ measured with current applied along [001]. Inset shows low-temperature data fitted to $\rho_0 + AT^2$; $\rho_0 = 113.8 \mu\Omega \text{ cm}$, and $A = 0.00173 \mu\Omega \text{ cm K}^{-2}$. b) Specific heat capacity of CoTe₂ as a function of temperature (black) and Debye model fit (Equation 1, red). The inset shows the measured $T < 7 \text{ K}$ C/T vs T^2 dependence (black) and linear fitting to Equation 2 (red). c) Magnetoresistance (MR) of CoTe₂ at indicated temperatures. Solid lines are fits of different functions to the data as described in the text. d) Hall resistivity versus magnetic field at indicated temperatures. Solid lines are straight line fits to the data.

degeneracy at one single point in the Brillouin zone, which can only appear on the Fermi level by accident (DP-0). The next level is a nodal line, that is, a line of Dirac points, which can cross the Fermi surface at isolated points (DP-1). An even stronger, and much less common, there is a nodal plane generating a line of Dirac points on the Fermi level (DP-2). In our case, we have all of those, plus a special Dirac point on the Fermi surface between S and R. Here, the Dirac degeneracy is protected not only when one component of the wave vector is changing (as in DP-1), or two components (DP-2), but all three components k_x , k_y , and k_z (DP-3). Only when two or more components are varied simultaneously, the degeneracy is lifted (see Section S4 and Figures S4 and S5, Supporting Information for details). This is the “strongest” Dirac point that can exist in a 3D system, and it occurs rather rarely in real systems.

Often, presence of the Dirac bands near the Fermi surface gives rise to unusual transport signatures. In clean semimetals, they may give rise to extremely large magnetoresistance (MR), quantum oscillations and non-zero Berry phase^[29–34] (it is to be noted that the extremely large MR and quantum oscillations in semimetals can have also a non-topological origin^[35–37]). However, a combination of multiple Dirac points and lines on the

Fermi surface (coming from nodal lines and planes passing through the entire Brillouin zone) have rarely been observed and their manifestation in the transport measurements have not been discussed. To this end, we carried out transport measurements on the single crystals of CoTe₂. Electrical resistivity of CoTe₂ as a function of temperature measured with current (I) along [001] is depicted in **Figure 2a** (black curve), which shows a metallic character in the entire temperature range between 1.8 and 300 K, consistent with the calculated electronic structure, and does not show any feature indicative of long range magnetic ordering. Specific heat capacity from 1.8 to 200 K is shown in **Figure 2b** (black curve), which shows a monotonic change with temperature not showing any sign of long range magnetic ordering as in the resistivity measurement. Although no long range magnetic ordering is observed in resistivity and heat capacity measurements, their analysis provide information on the average phonon frequency in terms of the Debye temperature, Θ_D . The formula for the specific heat as a function of temperature is

$$C(T) = 9R \left(\frac{T}{\Theta_D} \right)^3 \int_0^{\Theta_D/T} \frac{t^4 e^t}{(e^t - 1)^2} dt + \gamma T \quad (1)$$

where the first (Debye) term gives the phonon contribution to the specific heat, and R is the gas constant. The second term is the Sommerfeld electronic specific heat with the coefficient γ giving the mass-renormalized density of states. In the low temperature limit this simplifies to,

$$C(T) = AT^3 + \gamma T \quad (2)$$

where the first term is the contribution from acoustic phonons, $A = 12\pi^4 R/5\Theta_D^3$. Fitting both the full temperature range to Equation 1 (red curve in Figure 2b), as well as just the low temperature data to Equation 2 [inset in Figure 2(b)] yield similar results finding $\Theta_D = 275.4$ K and $\gamma = 14.22$ mJ mol⁻¹ K⁻¹ for Equation 1 and $\Theta_D = 273.1$ K and $\gamma = 12.45$ mJ mol⁻¹ K⁻¹ for Equation 2 and $T < 7$ K, indicating that the contribution from optical phonons at lower temperatures is small. This γ is to be compared with the Sommerfeld coefficient from the unrenormalized DFT density of states, $N(E_F) \approx 6.5$ states per eV f.u., $\gamma_0 \approx 7.6$ mJ mol⁻¹ K⁻¹, giving a mass renormalization between 60 and 90%; note that if this renormalization were due to electron–phonon coupling the material would have been a good superconductor, so we interpret this as the manifestation of critical spin fluctuations discussed below.

We further analyzed the temperature dependence of the resistivity in terms of the Bloch–Grüneisen (BG) formula,^[38] where the electrical resistivity is

$$\rho_{xx}(T) = \rho_0 + \rho_{ph}(T) \quad (3)$$

and ρ_0 is the residual resistivity at $T = 0$. The temperature-dependent term is given by refs. [38, 39],

$$\rho_{ph}(T) = \alpha_n \rho_{\Theta_R} \left(\frac{T}{\Theta_R} \right)^n \int_0^{\Theta_R/T} \frac{t^n}{(e^t - 1)(1 - e^{-t})} dt \quad (4)$$

where α_n is a coefficient describing the scattering rate, Θ_R is the BG temperature, which is typically close, albeit not always equal to the Debye temperature, ρ_{Θ_R} is the residual resistivity at $T = \Theta_R$, and the exponent n takes the value of 2, 3, or 5 depending on the specifics of the electronic interactions present within the material.^[40–42] For standard acoustic phonon scattering, the exponent n is 5 and the coefficient α_5 is 4.225. Inserting these values for acoustic phonons as well as fixing the $\Theta_R = \Theta_D$ of 275.4 K, yields a temperature dependent resistivity in close agreement with experiment. It is known that the resistivity can observe a T^2 dependence in the presence of high paramagnetism and large electronic specific heat,^[42] and further, the assumption that $\Theta_R = \Theta_D$ isn't strictly true.^[38] This T^2 dependence would take the same form as Equation 4, with $n = 2$, and where α_2 is a constant coefficient describing the scattering rate of the T^2 behavior. We find the T^2 dependence at low temperature much more accurately reflects the temperature dependence of resistivity (inset in Figure 2a).

The magnetoresistance (MR), defined as $[\rho(B) - \rho(B = 0)]/\rho(B = 0)$, for I along [001] and the magnetic field B along [110] between 1.8 and 30 K, is shown in Figure 2c. The MR in CoTe₂ is extremely small but at lower temperatures $T < 10$ K it is linear in magnetic field, and non-saturating. The linear behavior gradually changes with temperature. A $B^{1.31}$ dependence is observed at 10 K, $B^{1.44}$ dependence at 20 K, and finally exhibiting a more conventional B^2 dependence at 30 K. We verified this behavior in more than one samples from different

growth batches (see Figure S6, Supporting Information). The linear MR is an interesting property and has been observed in many material systems.^[43,–52] However, it is frequently observed and used as evidence for materials exhibiting topological features in their electronic structure.^[43,44,48,50–56] One prevalent non-topological reason for the linear MR is disorder.^[46,47,54,57] But in such a case, the linear MR usually spans a large temperature range unlike the quickly attained quadratic behavior at 30 K in CoTe₂. Another widely observed reason for the linear MR is an admixture of a component of the Hall resistivity (which depends linearly on the magnetic field) to the longitudinal resistance caused by inhomogeneities such as density or sample thickness variations.^[58] Such variations give rise to a gradient of the (transverse) Hall voltage in the longitudinal direction that will naturally be picked up in measurements of the longitudinal resistance, therefore giving rise to a linear component in the magnetoresistance. In CoTe₂, the Hall resistivity is linear at all temperatures measured (Figure 2d) and its influence only at the lower temperatures, where the MR is actually larger, is not consistent with this mechanism. In fact, thermal conductivity measured as a function of temperature (see Figure S7, Supporting Information) shows a sharp drop below about 30 K indicating that Umklapp process is frozen out below this temperature and thus the effect of phonon scattering is smaller at the temperature range where linear MR is observed, consistent with the conclusion drawn from the analysis of the heat capacity data. This observation is indicative that with the increase in temperature phonons may play a role in suppressing the linear MR in CoTe₂. As the magnetotransport of such a system with the coexisting nodal points, lines and planes have never been measured and analyzed before, this anomalous magnetotransport behavior of CoTe₂ calls for further theoretical and experimental investigations.

To characterize the magnetism in CoTe₂ we performed DC magnetic measurements. The blue curve in Figure 3a (plotted in the left axis) shows magnetic susceptibility as a function of temperature between 1.8 and 375 K. The susceptibility increases slowly with decreasing temperature but does not show a sign of a long-range ordering, consistent with resistivity and heat capacity measurements. It neither diverges at lower temperatures as in normal paramagnetic materials. It is an indication that the material tends to order but the ordering is somehow suppressed (by strong spin fluctuations, which we will discuss below). Inverse susceptibility after subtracting a small diamagnetic background (χ_0 of -1.58×10^{-5} cm³ mol⁻¹ F.U.⁻¹) determined from the Curie–Weiss fit to the susceptibility above 50 K (indicated by the red dashed line) is plotted in the right hand axis of Figure 3a. Thus obtained inverse susceptibility is linear over a wide range of temperature (down to 25 K) and its fitting to the Curie–Weiss law (red solid line in Figure 3a):

$$\frac{1}{(\chi - \chi_0)} = \frac{(T - T_\theta)}{C} \quad (5)$$

where χ is the spin susceptibility, C is the Curie constant, and T_θ is the Curie–Weiss temperature, yields the effective moment ($\mu_{\text{eff}} = \sqrt{8C}$) of 1.940 μ_B per Co. This agrees reasonably well with the theoretical $\mu_{\text{eff}} = 2\mu_B \sqrt{S(S+1)}$ of 1.732 μ_B per Co for the low-spin state ($S = 1/2$) Co⁴⁺. This leaves room for a g-factor of 2.24, indicating that the effect of spin–orbit coupling is weak

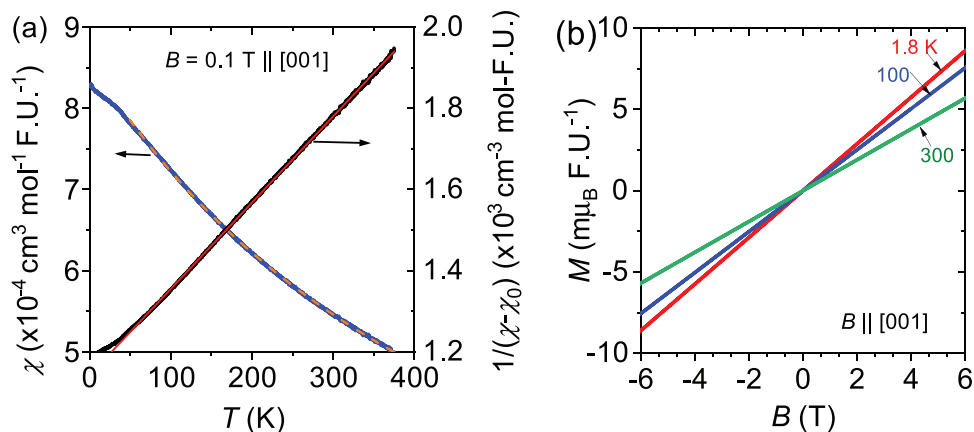


Figure 3. a) DC magnetic susceptibility ($\chi = M/B$) as a function of temperature for $B = 0.1$ T along the c -axis (left axis). The dashed line shows a fit to the Curie–Weiss law between 50 and 375 K, yielding $\chi_0 = -1.585 \times 10^{-5} \text{ cm}^3 \text{ mol}^{-1} \text{ F.U.}^{-1}$. $1/(\chi - \chi_0)$ vs T is plotted in the right axis (black line). The red solid line is a Curie–Weiss fit. b) Magnetization versus magnetic field at the indicated temperatures.

(cf., Figure S4, Supporting Information). T_θ obtained from the x -intercept is ≈ 30 K. The sizable positive value indicates the presence of ferromagnetic correlations. Magnetization data (M vs B) depicted in Figure 3b is linear at all temperatures between 1.8 and 300 K indicating that the paramagnetism observed at room temperature, unusually, persists down to the lowest measured temperatures. The fact that despite the large T_θ the material does not order down to ≈ 1 K indicates strong spin fluctuations.

Additional insight can be gained from the density functional theory (DFT) calculations. Being mean-field by nature, DFT calculations do not account for fluctuation-driven suppression of magnetic order. Correspondingly, calculating the ferromagnetic total energy in DFT as a function of spin magnetization yields a ferromagnetic ground state with a moment of $M = 0.6 \mu_B/\text{Co}$, also corresponding to $S = 1/2$ (with a typical for DFT hybridization reduction), whose total stabilization energy is however only ≈ 6 meV/Co), as shown in Figure 4. The effect of fluctuations

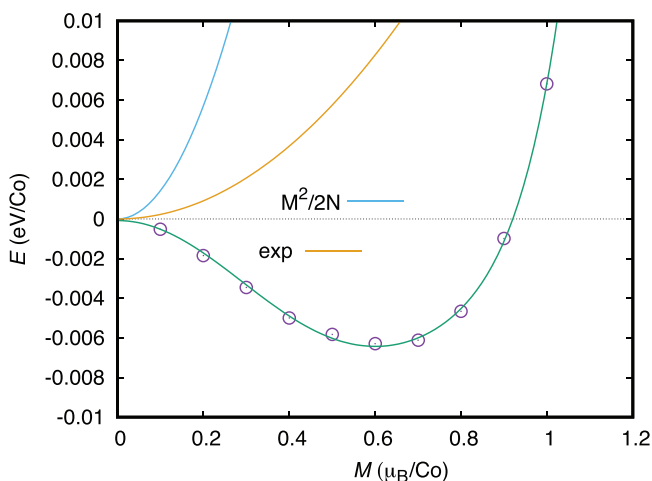


Figure 4. DFT calculation predicting a ferromagnetic ground state (purple points). The blue line is the parabola corresponding to the Pauli susceptibility with the calculated density of states N . The orange line is obtained from the Moriya's SCRT formula with the spin fluctuations amplitude adjusted to match the experimental zero temperature susceptibility (see the text for more details).

can be approximated by means of Moriya's SCRT.^[23,59] If the DFT energy is expanded as a polynomial in M ,

$$E = a + bM^2 + cM^4 + dM^6 + eM^8 \dots \quad (6)$$

and there are Gaussian fluctuations of the magnetic moment with an average squared amplitude ξ^2 , then, in SCRT, the renormalized energy is given by

$$E = a + (b + 5c\xi^2 + 35d\xi^4 + 35e\xi^6)M^2 + \dots \quad (7)$$

and the renormalized susceptibility is, as usually, $\chi^{-1} = \partial^2 E / \partial M^2$. Typically, Moriya's parameter ξ is comparable with, or somewhat larger than the equilibrium DFT value. Fitting our DFT calculations (the green line in Figure 4), and assuming fluctuations with $\xi \approx 0.71 \mu_B$, consistent with the DFT moment of $0.6 \mu_B$, we can reproduce the experimental susceptibility at $T = 0$. Thus, CoTe_2 is a material where ferromagnetic order is suppressed by strong spin fluctuations, leaving the ground state on the verge of a magnetic quantum critical phase transition.

3. Conclusion

Our measurements and calculations suggest that CoTe_2 sports a unique combination of a quantum criticality and multiple nodal Dirac lines. The ferromagnetic order is wholly suppressed, maintaining paramagnetic behavior down to the lowest measured temperatures due to strong spin fluctuation. The calculated bands show that this material has potential for harboring new topological physics, as CoTe_2 hosts both nodal Dirac lines, and more conventional Dirac points directly on the Fermi surface, within a single material on the verge of quantum criticality. This study should prompt future investigations into system, for instance, by probing the Dirac dispersions via photoemission and quantum oscillations. A quantum critical point may be reached by doping or pressure to provide further insight into the interplay between magnetism and topological fermions.

4. Experimental Section

Single-Crystal Growth and X-ray Diffraction. Single crystals of CoTe_2 were grown by molten metal flux method with Te as a self flux. Co powder (Alfa Aesar; 99.998%), and Te shots (Alfa Aesar; 99.9999%), were loaded in a 2 mL aluminum oxide crucible in a molar ratio of 1:19. The crucible was then sealed in a fused silica ampule under vacuum. The sealed ampule was heated to 800 °C over 12 h, homogenized at 800 °C for 10 h. The furnace was then quickly cooled to 760 °C in 2 h followed by slow cooling to 580 °C over 140 h. Once the furnace reached 580 °C, the excess flux was decanted from the crystals using a centrifuge. Well-faceted rectangular crystals as large as 30 mg were obtained. The crystal structure of the compound was first verified by X-ray powder diffraction at room temperature using a Rigaku MiniFlex diffractometer and then by single-crystal X-ray diffraction. A few crystals from each growth batch were ground into powder, and X-ray diffraction patterns were collected on those powder samples. Rietveld refinement^[60] of powder X-ray pattern was performed using FullProf software.^[61] Single-crystal X-ray diffraction data of CoTe_2 were collected on a piece of a representative single crystal at room temperature using a Rigaku XtaLAB Synergy-i diffractometer with the HyPix-Bantam direct photon-counting detector. The single-crystal was glued on a loop and mounted on the goniometer head of the diffractometer. The crystal structure of CoTe_2 was solved with space group *Pnnm* and refined with the SHELX program.^[62]

STEM Measurements. An FEI Helios NanoLab 660 DualBeam (SEM/FIB) system was used to prepare cross-sectional TEM samples. Electron-beam-induced deposition of Pt was initially deposited on top of the materials to protect the sample surface, followed by 3 μm ion-beam induced Pt deposition. To reduce Ga ion damage, 2 kV Ga-ion beam was applied to thin the lamella in the final step. An FEI Titan 80-300 STEM/TEM equipped with a probe spherical-aberration corrector was employed to conduct atomic resolved scanning transmission electron microscopy (STEM) imaging.

Raman Measurements. Raman measurements of CoTe_2 single crystals were performed at room temperature in a backscattering geometry. The sample was excited by a 532 nm laser focused through a 0.75 NA objective lens with 40 \times magnification. The laser power was measured to be 200 μW before the objective. Scattered light was collected through the same lens and directed to an imaging spectrograph. Rejection of the laser is accomplished using a pair of long pass dielectric filters that allow measurement of Raman scattered light down to 75 cm^{-1} .

Magnetic, Transport, and Thermal Measurements: Electronic transport measurements were conducted within the 9-T Quantum Design PPMS with the DC resistivity option. Samples were polished to dimensions of approximately 1.00 \times 0.40 \times 0.12 mm with the long axis corresponding to the [001] direction. An excitation current of 4 mA was used for all measurements. Electrical contacts were affixed using Epotek H20E silver epoxy and 25 μm Pt wires with typical contacts resistances of $\approx 10 \Omega$, such that current was directed along the [001] direction. In magnetoresistance measurements, the contact misalignment was corrected by field symmetrizing (for MR) and antisymmetrizing (for Hall) the measured data. Magnetization measurements were made using a Quantum Design VSM SQUID in the field-cooled mode. Heat capacity was measured with the Quantum Design PPMS. The thermal conductivity was measured via the Quantum Design PPMS Thermal Transport Option (TTO) where the sample was polished to a rectangular bar and mounted with the standard TTO thermometer shoes. The sample geometry yielded a cross-sectional area of 0.747 mm^2 with thermometer lead separation of 1.628 mm. The applied heat current was directed along the c-axis of the sample with the heat pulses maintained at 3% of the sample temperature for each temperature setpoint measured.

First-Principles Calculations. Most calculations were performed using the all-electron linearized augmented plane wave code WIEN2k^[63] with gradient approximation for the exchange-correlation energy,^[64] including the results shown in Figures 1 and 3. For control purposes, some calculations were performed using projected augmented wave pseudo-potential code VASP.^[65] Figure S4 (Supporting Information) was generated using the Full Potential Local Orbitals (FPLO)^[66] package

(agreement of the results with WIEN2k was verified). For all calculations the experimental crystal structure was used. A k-mesh of 60³ divisions was used to generate Figure 1.

Supporting Information

Supporting Information is available from the Wiley Online Library or from the author.

Acknowledgements

The authors thank Binghai Yan for insightful discussions. N.J.G. acknowledges the support from the NSF CAREER award DMR-2143903. Crystal growth part of the work at George Mason University was supported by the U.S. Department of Energy, Office of Science, Basic Energy Sciences, Materials Science and Engineering Division. I.I.M. acknowledges support from the U.S. Department of Energy through the grant no. DE-SC0021089. M.P.G. acknowledges the Alexander von Humboldt Foundation, Germany and IFW-Dresden, Germany for the equipment grants. R.G. thanks UGC-Nepal for the fellowship with award number MRS-77/78 S & T -119. Magnetic characterization at G.U. have been supported by the NSF (ECCS-2151809). The acquisition of a Magnetic Property Measurements System (MPMS3, Quantum Design) at G.U. used herein was supported by the NSF (DMR-1828420). H.Z. acknowledges support from the U.S. Department of Commerce, NIST under financial assistance award 70NANB19H138. A.D. acknowledges support from the Material Genome Initiative funding allocated to NIST. J.J. and P.M.V. acknowledge support from the NSF CAREER award DMR-1847782.

Conflict of Interest

The authors declare no conflict of interest.

Data Availability Statement

The data that support the findings of this study are available from the corresponding author upon reasonable request.

Keywords

Dirac fermions, nodal line metals, quantum criticality, spin fluctuations, topological materials

Received: January 19, 2023

Published online:

- [1] N. P. Armitage, E. J. Mele, A. Vishwanath, *Rev. Mod. Phys.* **2018**, *90*, 15001.
- [2] A. A. Burkov, M. D. Hook, L. Balents, *Phys. Rev. B* **2011**, *84*, 235126.
- [3] Y. Kim, B. J. Wieder, C. L. Kane, A. M. Rappe, *Phys. Rev. Lett.* **2015**, *115*, 036806.
- [4] T. Bzdušek, Q. Wu, A. Rüegg, M. Sigrist, A. A. Soluyanov, *Nature* **2016**, *538*, 75.
- [5] J. W. Rhim, Y. B. Kim, *Phys. Rev. B* **2015**, *92*, 045126.
- [6] Z. Zhu, G. W. Winkler, Q. Wu, J. Li, A. A. Soluyanov, *Phys. Rev. X* **2016**, *6*, 031003.
- [7] K.-H. Ahn, W. E. Pickett, K. W. Lee, *Phys. Rev. B* **2018**, *98*, 035130.

- [8] N. J. Ghimire, M. A. Khan, A. S. Botana, J. S. Jiang, J. F. Mitchell, *Phys. Rev. Mater.* **2018**, 2, 081201(R).
- [9] J. F. Khoury, A. J. E. Rettie, M. A. Khan, N. J. Ghimire, I. Robredo, J. E. Pfluger, K. Pal, C. Wolverton, A. Bergara, J. S. Jiang, L. M. Schoop, M. G. Vergniory, J. Mitchell, D. Y. Chung, M. G. Kanatzidis, *J. Am. Chem. Soc.* **2019**, 141, 19130.
- [10] M. J. Gilbert, *Commun. Phys.* **2021**, 4, 70.
- [11] M. M. H. Polash, S. Yalameha, H. Zhou, K. Ahadi, Z. Nourbakhsh, D. Vashaee, *Mater. Sci. Eng., R* **2021**, 145, 100620.
- [12] N. Kumar, S. N. Guin, K. Manna, C. Shekhar, C. Felser, *Chem. Rev.* **2021**, 121, 2780.
- [13] A. Leonhardt, M. M. Hirschmann, N. Heinsdorf, X. Wu, D. H. Fabini, A. P. Schnyder, *Phys. Rev. Mater.* **2021**, 5, 124202.
- [14] G. Xu, H. Weng, Z. Wang, X. Dai, Z. Fang, *Phys. Rev. Lett.* **2011**, 107, 186806.
- [15] Z. Yan, Z. Wang, *Phys. Rev. Lett.* **2016**, 117, 087402.
- [16] G. Bian, T.-r. Chang, R. Sankar, S.-y. Xu, H. Zheng, T. Neupert, C.-k. Chiu, S.-m. Huang, G. Chang, I. Belopolski, D. S. Sanchez, M. Neupane, N. Alidoust, C. Liu, B. Wang, C.-c. Lee, H.-t. Jeng, C. Zhang, Z. Yuan, S. Jia, A. Bansil, F. Chou, H. Lin, M. Z. Hasan, *Nat. Commun.* **2016**, 7, 10556.
- [17] N. B. Kopnin, T. T. Heikkil, G. E. Volovik, *Phys. Rev. B* **2011**, 83, 220503.
- [18] G. E. Volovik, *The Universe in a Helium Droplet*, Oxford University Press, Oxford, UK **2012**.
- [19] G. E. Volovik, in *Momentum Space in Quantum Analogues: From Phase Transitions to Black Holes and Cosmology, Lecture Notes in Physics*, (Eds.: W. G. Unruh, R. Schützhold), Springer, Berlin Heidelberg, Germany **2007**, pp. 31–73.
- [20] D. J. Singh, I. I. Mazin, *Phys. Rev. Lett.* **2002**, 88, 187004.
- [21] J. R. Stewart, B. D. Rainford, R. S. Eccleston, R. Cywinski, *Phys. Rev. Lett.* **2002**, 89, 186403.
- [22] I. I. Mazin, D. J. Singh, A. Aguayo, in *Physics of Spin in Solids: Materials, Methods and Applications*, Springer, Dordrecht **2004**, pp. 139–154.
- [23] T. Moriya, *Spin Fluctuations in Itinerant Electron Magnetism*, Springer Series in Solid-State Sciences, Vol. 56, Springer Verlag, Berlin/Heidelberg, Germany **1985**.
- [24] G. Brostigen, A. Kjekshus, *Acta Chem. Scand.* **1970**, 24, 1925.
- [25] J. A. R. Cheda, E. F. Westrum, F. Gronvold, *Monatsh. Chem.* **1986**, 117, 1223.
- [26] H. Ma, W. Dang, X. Yang, B. Li, Z. Zhang, P. Chen, Y. Liu, Z. Wan, Q. Qian, J. Luo, K. Zang, X. Duan, X. Duan, *Chem. Mater.* **2018**, 30, 8891.
- [27] M. Muhler, W. Bensch, M. Schur, *J. Phys.: Condens. Matter* **1998**, 10, 2947.
- [28] NIST disclaimer: Certain commercial equipment, instruments, or materials are identified in this paper in order to specify the experimental procedure adequately. Such identifications are not intended to imply recommendation or endorsement by the National Institute of Standards and Technology (NIST), nor it is intended to imply that the materials or equipment identified are necessarily the best available for the purpose
- [29] M. N. Ali, J. Xiong, S. Flynn, J. Tao, Q. D. Gibson, L. M. Schoop, T. Liang, N. Haldolaarachchige, M. Hirschberger, N. P. Ong, R. J. Cava, *Nature* **2014**, 514, 205.
- [30] N. J. Ghimire, Y. Luo, M. Neupane, D. J. Williams, E. D. Bauer, F. Ronning, *J. Phys.: Condens. Matter* **2015**, 27, 152201.
- [31] T. Liang, Q. Gibson, M. N. Ali, M. Liu, R. J. Cava, N. P. Ong, *Nat. Mater.* **2015**, 14, 280.
- [32] N. J. Ghimire, A. S. Botana, D. Phelan, H. Zheng, J. F. Mitchell, *J. Phys.: Condens. Matter* **2016**, 28, 19.
- [33] A. A. Burkov, *Phys. Rev. Lett.* **2014**, 113, 187202.
- [34] H. Murakawa, M. S. Bahramy, M. Tokunaga, Y. Kohama, C. Bell, Y. Kaneko, N. Nagaosa, H. Y. Hwang, Y. Tokura, *Science* **2013**, 342, 1490.
- [35] Y. Luo, R. D. McDonald, P. F. Rosa, B. Scott, N. Wakeham, N. J. Ghimire, E. D. Bauer, J. D. Thompson, F. Ronning, *Sci. Rep.* **2016**, 6, 27294.
- [36] S. Sun, Q. Wang, P.-J. Guo, K. Liu, H. Lei, *New J. Phys.* **2016**, 18, 082002.
- [37] J. He, C. Zhang, N. J. Ghimire, T. Liang, C. Jia, J. Jiang, S. Tang, S. Chen, Y. He, S. K. Mo, C. C. Hwang, M. Hashimoto, D. H. Lu, B. Moritz, T. P. Devereaux, Y. L. Chen, J. F. Mitchell, Z. X. Shen, *Phys. Rev. Lett.* **2016**, 117, 267201.
- [38] J. M. Ziman, *Electrons and Phonons: The Theory of Transport Phenomena in Solids*, Oxford University Press, Oxford, UK **2001**.
- [39] A. Bid, A. Bora, A. K. Raychaudhuri, *Phys. Rev. B* **2006**, 74, 035426.
- [40] D. Cvijovic, *Adv. Theor. Math. Phys.* **2011**, 166, 37.
- [41] A. H. Wilson, *Proc. R. Soc. Lond. A* **1938**, 157, 580.
- [42] W. G. Barber, *Proc. R. Soc. Lond. A* **1937**, 158, 383.
- [43] W. Zhang, R. Yu, W. Feng, Y. Yao, H. Weng, X. Dai, Z. Fang, *Phys. Rev. Lett.* **2011**, 106, 156808.
- [44] C. M. Wang, X. L. Lei, *Phys. Rev. B* **2012**, 86, 035442.
- [45] T. Khouri, U. Zeitler, C. Reichl, W. Wegscheider, N. E. Hussey, S. Wiedmann, J. C. Maan, *Phys. Rev. Lett.* **2016**, 117, 256601.
- [46] N. V. Kozlova, N. Mori, O. Makarovskiy, L. Eaves, Q. D. Zhuang, A. Krier, A. Patané, *Nat. Commun.* **2012**, 3, 1097.
- [47] R. Xu, A. Husmann, T. F. Rosenbaum, M.-L. Saboungi, J. E. Enderby, P. B. Littlewood, *Nature* **1997**, 390, 57.
- [48] Y. Zhao, H. Liu, J. Yan, W. An, J. Liu, X. Zhang, H. Wang, Y. Liu, H. Jiang, Q. Li, Y. Wang, X.-z. Li, D. Mandrus, X. C. Xie, M. Pan, J. Wang, *Phys. Rev. B* **2015**, 92, 041104.
- [49] J. Feng, Y. Pang, D. Wu, Z. Wang, H. Weng, J. Li, X. Dai, Z. Fang, Y. Shi, L. Lu, *Phys. Rev. B* **2015**, 92, 081306(R).
- [50] M. Novak, S. Sasaki, K. Segawa, Y. Ando, *Phys. Rev. B* **2015**, 91, 041203(R).
- [51] H. Tang, D. Liang, R. L. J. Qiu, X. P. A. Gao, *ACS Nano* **2011**, 5, 7510.
- [52] G. M. Gusev, E. B. Olshanetsky, Z. D. Kvon, N. N. Mikhailov, S. A. Dvoretzky, *Phys. Rev. B* **2013**, 87, 081311(R).
- [53] A. A. Abrikosov, *Phys. Rev. B* **1998**, 58, 2788.
- [54] J. Hu, T. F. Rosenbaum, *Nature* **2008**, 7, 697.
- [55] C. Fang, Y. Chen, H.-y. Kee, L. Fu, *Phys. Rev. B* **2015**, 92, 081201.
- [56] I. A. Leahy, Y.-p. Lin, P. E. Siegfried, A. C. Treglia, J. C. W. Song, R. M. Nandkishore, M. Lee, *Proc. Natl. Acad. Sci. USA* **2018**, 115, 10570.
- [57] M. M. Parish, P. B. Littlewood, *Nature* **2003**, 426, 162.
- [58] G. J. C. L. Bruls, J. Bass, A. P. van Gelder, H. van Kempen, P. Wyder, *Phys. Rev. Lett.* **1981**, 46, 553.
- [59] P. Larson, I. I. Mazin, D. J. Singh, *Phys. Rev. B* **2004**, 69, 064429.
- [60] L. B. McCusker, R. B. Von Dreele, D. E. Cox, D. Louër, P. Scardi, *J. Appl. Cryst.* **1999**, 32, 36.
- [61] J. Rodriguez-Carvajal, *Phys. B* **1993**, 192, 55.
- [62] G. M. Sheldrick, *Acta Crystallogr.* **2015**, C71, 3.
- [63] P. Blaha, K. Schwarz, G. K. H. Medsen, D. Kvasnicka, J. Luitz, *An Augmented Plane Wave Plus Local Orbitals Program for Calculating Crystal Properties*, Vienna University of Technology, Vienna, Austria **2001**.
- [64] J. P. Perdew, K. Burke, M. Ernzerhof, *Phys. Rev. Lett.* **1996**, 77, 3865.
- [65] G. Kresse, J. Furthmüller, *Phys. Rev. B* **1996**, 54, 11169.
- [66] K. Koepnik, H. Eschrig, *Phys. Rev. B* **1999**, 59, 1743.